Simulation of the Three-Dimensional Two-Phase Flow in Stirred Extraction Columns by Lagrangian-Eulerian Method

X. Y. You[a]* and Xia Xiao[b]
[a]School of Environmental Science and Engineering, Tianjin University, Tianjin 300072, P.R. China
[b]School of Electrical and Information Engineering, Tianjin University, Tianjin 300072, P.R. China

Original scientific paper
Received: April 28, 2004
Accepted: November 1, 2004

The two-phase flow field of agitated extraction columns is simulated with the help of computational fluid dynamics (CFD). In this paper, the continuous phase is described by Eulerian model and the dispersed phase (drops) is simulated by Lagrangian model. The interaction of rotor and baffle is considered by applying the multiple reference frame concepts.

The distributions of the dispersed phase (drops) and the flow field of continuous phase can be obtained by the Lagrangian-Eulerian method described here. Numerical results show that the Lagrangian-Eulerian method can be adopted to evaluate the performance and optimize the design of extraction column.

Key words:
Stirred extraction column, Lagrangian-Eulerian method, computational fluid dynamics, two-phase flow

Introduction

Agitated extraction columns are widely used in the process industry to separate the components in homogeneous liquid mixtures. Although extraction columns have been used in industry for many years, and their performance is relatively sound, there is deficiency of reliable design and scale-up procedures. A large amount of money may be lost as a consequence of the uncertainties in the design of extraction columns. It is believed that a significant improvement on extraction column design can be obtained by developing appropriate numerical models, in which the real flow field of the column is taken into account. An effort has been made during the past few years to develop predictive methods based on computational fluid dynamics (CFD), which is capable to provide detailed information of the turbulence flow field and further details on the mass transfer between phases. With the help of CFD, some successful examples of optimizing reactors have appeared in literatures, such as *Krishna* and *Baten*[1] for bubble column reactors, *Yu* et al.[2] for distillation sieve towers and *You*[3] for distillation sieve towers by considering the mass transfer between phases.

Some studies, which have appeared in literatures, are focused on the numerical simulation of single-phase flow field (only considering the continuous phase) in stirred vessels. *Fei* et al.[4] made studies in the single-phase flow velocity field of rotating disc contactors by CFD and by Laser Doppler Velocimeter (LDV) measurement. Their numerical results were in fair agreement with the experimental ones.

Sun et al.[5] adopted an anisotropic stress model to predict the turbulent flow field and turbulent characteristics generated by a Rushton disc turbine. Their numerical results were compared with the experimental data and the results of standard $k-\varepsilon$ turbulence model. It was found that the anisotropic stress model could give a better prediction than the standard $k-\varepsilon$ turbulence model. *Bartels* et al.[6] realized the computation of stirred vessel flows on a two-parallel-vector-computer architecture that is able to provide the computer power needed for large-scale flow predictions. *You* and *Bart*[7] adopted four categories of the current-state of art high-resolution Reynolds-averaged turbulence models (i.e. the standard $k-\varepsilon$ model (KE), the RNG $k-\varepsilon$ model (RNGKE), the realizable $k-\varepsilon$ model (RKE) and the Reynolds stress model (RSM)) to simulate the continuous phase flow field of the stirred extraction column. Their results suggested that the realizable $k-\varepsilon$ model (RKE) is the best choice because of its high accuracy and less consumed computer resources (computer CPU time and memory).

For Lagrangian-Eulerian simulation, most of studies were involved in the field of fluidized beds.

* To whom correspondence should be addressed.
Email: *xyyou@tju.edu.cn* Tel: +86–22–27403561, Fax: +86–22–27402555

Wachem et al.[8] validated the two-dimensional Lagrangian-Eulerian simulation of gas-solid fluidized beds by comparing it with the experimental data. They found that the numerical simulations in the qualitative trends correctly reproduced the experiments. *Li* et al.[9] presented a new approach, which is to combine Lagrangian-Eulerian method and volume-of-fluid method, to simulate the gas-liquid-solid flow field in a fluidized bed. Their results showed good agreement with the experimental findings.

For an agitated Kuehni-type miniplant extractor, a scale-up method based on CFD is still needed to reduce the uncertainties in its design and to optimize its performance. To achieve this objective, a Lagrangian-Eulerian method is firstly presented to investigate the hydrodynamic behavior of the liquid-liquid two-phase flow in Kuehni-type extraction columns. In this study, we assume the dispersed phase (toluene drops) as solid drops for its high interfacial tension with respect to water. Because of the sufficiently low drop volume fraction (less than 5 % for average), the effects of particle collision are neglected in all calculations. The mass transfer between the liquid-liquid phases in the extraction column is not considered in this study and it will be our next research topic in the future.

The description of Lagrangian-Eulerian method

The continuous phase

The governing equations of continuous phase of multiphase flow can be derived from the N-S equations for single-phase flow. Considering the existence of dispersed particles, a volume-averaged technique is applied to develop the controlling equations of mass and momentum conservation of continuous phase.

The volume-averaged continuity equation for incompressible continuous liquid phase is

$$\frac{\partial \varepsilon_1}{\partial t} + \nabla \cdot (\varepsilon_1 \boldsymbol{u}_1) = 0.$$

And the volume-averaged momentum equation is

$$\rho_1 \frac{\partial (\varepsilon_1 \boldsymbol{u}_1)}{\partial t} + \rho_1 \nabla \cdot (\varepsilon_1 \boldsymbol{u}_1 \boldsymbol{u}_1) = \\ = -\nabla p + \nabla \cdot [\mu_1 \varepsilon_1 (\nabla \boldsymbol{u}_1 + (\nabla \boldsymbol{u}_1)^{\mathrm{T}})] + \varepsilon_1 \rho_1 \boldsymbol{g} + \boldsymbol{F}. \quad (2)$$

where e_1, $\boldsymbol{u}_1$, ρ_1 and μ_1 are the volume fraction, velocity, density and viscosity of continuous loquid phase, respectively. $\boldsymbol{g}$ is the gravity constant. $\boldsymbol{F}$ is the body force acting on the continuous phase from the motion of particles. It consists of drag force, the added mass force and addition force. The concrete expression of $\boldsymbol{F}$ can be found in the following equation (4). In equations (1) and (2), the volume fraction ε_1 is approximated to 1 for low dispersed phae concentration in our calculation. Then we can set $\varepsilon_1 = 1$ with safety.

Particle tracking

The path of each individual particle is calculated by Lagrangian model. The calculation of particle moving path consist of two steps. One step is the calculation of the motion of particles. The other is the consideration of the collision of a particle with another particle. In all our calculation cases, the particle volume fraction is sufficiently small, which is about 5 % for average. Then the effects of particle collision can be neglected in all calculation. The motion of individual particles is completely determined by Newton's second law of motion as

$$\frac{\mathrm{d}\boldsymbol{u}_\mathrm{p}}{\mathrm{d}t} = \boldsymbol{F} + \boldsymbol{g}\frac{\rho_\mathrm{p} - \rho_1}{\rho_\mathrm{p}} \quad (3)$$

where, $\boldsymbol{F}$ is written as

$$\boldsymbol{F} = F_\mathrm{D}(\boldsymbol{u}_1 - \boldsymbol{u}_\mathrm{p}) + \frac{\rho_1}{2\rho_\mathrm{p}}\frac{\mathrm{d}}{\mathrm{d}t}(\boldsymbol{u}_1 - \boldsymbol{u}_\mathrm{p}) + \boldsymbol{F}_\mathrm{A}. \quad (4)$$

Here, ρ_p and $\boldsymbol{u}_\mathrm{p}$ are the density and velocity of the dispersed drops, respectively. The terms at the right hand side of equation (4) are drag force, "virtual mass" force and the addition force.

$F_\mathrm{D}(\boldsymbol{u}_1 - \boldsymbol{u}_\mathrm{p})$ is the drag force per unit particle mass and F_D can be written as $\frac{18\mu_1}{\rho_\mathrm{p} d_\mathrm{p}^2}\frac{C_\mathrm{D} Re_\mathrm{p}}{24}$. Here, d_p is the diameter of the drop. $Re_\mathrm{p} = \frac{\rho_1 d_\mathrm{p} |\boldsymbol{u}_\mathrm{p} - \boldsymbol{u}_1|}{\mu_1}$ is the relative particle Reynolds number. C_D is the drag coefficient.

Liquid drops remain nearly spherical at moderate Reynolds number (e.g,, at Re = 500) if surface tension force is sufficiently strong, see *Clift* et al.[10] For our calculation, the interfacial tension of toluene against water is large. Then, we assume the liquid drops are spherical. The drag coefficient for liquid drops is adopted by the suggestion of *Clift* et al.[10] as

$$C_\mathrm{D} = \frac{16}{Re_\mathrm{p}} \quad (0 < Re_\mathrm{p} < 1.5), \quad (5a)$$

$$C_\mathrm{D} = 14.9\, Re_\mathrm{p}^{-0.78} \quad (1.5 < Re_\mathrm{p} < 4), \quad (5b)$$

$$C_D = \frac{3.05(783\kappa^2 + 2142\kappa + 1080)}{(60+29\kappa)(4+3\kappa)} Re_p^{-0.74} \quad (4 < Re_p < 100), \tag{5c}$$

here, $\kappa = \frac{\mu_p}{\mu_l}$ is the viscosity ratio of the liquid drop to the continuous phase liquid. The κ value reflects the intensity of internal circulation inside the liquid drop. For a large κ value, the internal circulation is negligible.

The addition force $\boldsymbol{F}_A$ represents the force from pressure gradient and fluid rotation and $\boldsymbol{F}_A = (F_{Ar}, F_{A\theta}, F_{Az})$ is written as)

$$F_{Ar} = \frac{\rho_l}{\rho_p} u_{pr} \frac{\partial u_{lr}}{\partial r} + \left(1 - \frac{\rho_l}{\rho_p}\right)\Omega_z^2 r + 2\Omega_z\left(u_{p,\theta} - \frac{\rho_l}{\rho_p} u_{l\theta}\right), \tag{6a}$$

$$F_{A\theta} = \frac{\rho_l}{\rho_p} u_{p\theta} \frac{\partial u_{l\theta}}{r\partial\theta} + 2\Omega_z\left(u_{pr} - \frac{\rho_l}{\rho_p} u_{lr}\right), \tag{6b}$$

$$F_{Az} = \frac{\rho_l}{\rho_p} u_{pz} \frac{\partial u_{lz}}{\partial z}, \tag{6c}$$

here $\boldsymbol{u}_l$ and $\boldsymbol{u}_p$ are denoted as ($\boldsymbol{u}_{lr}$, $\boldsymbol{u}_{l\theta}$, $\boldsymbol{u}_{lz}$) and ($\boldsymbol{u}_{pr}$, $\boldsymbol{u}_{p\theta}$, $\boldsymbol{u}_{pz}$), respectively.

The couple of the discrete and continuous phases

As the trajectory of a particle is computed, the lose of momentum of particle can be incorporated in the sequent continuous phase calculation. Notice should be made that no mass exchange is considered between the particle and the continuous phase here. While the continuous phase has an impact on the discrete (dispersed) phase (particle), this impact is also incorporated in next particle trajectory calculation. This two-way coupling is accomplished by alternately solving the discrete and continuous phase equations until the solutions in both phases have converged to preconcerted relative errors.

The momentum transfer from the continuous phase to the discrete phase is computed by examining the change of a particle momentum as the particle passes through the continuous phase. The momentum change is computed as

$$\boldsymbol{F} = \Sigma\left[\frac{18\mu_l C_D Re}{24\rho_p d_p^2}(\boldsymbol{u}_p - \boldsymbol{u}_l) + \boldsymbol{F}_{other}\right] Q_p \Delta t. \tag{7}$$

Here $\boldsymbol{F}_{other}$ is all other interaction forces, Q_p is the mass flow rate of the particles and Δt is the time step. This momentum exchange appears as a momentum sink in the continuous phase momentum equations when the continuous phase flow field is computed.

Implementation of Lagrangian-Eulerian method

For a coupled approach, the implementation of Lagrangian-Eulerian method is outlined as following:

– Solve the continuous phase flow field (prior to the introduction of the discrete phase).

– Introduce the discrete phase by calculating the particle trajectories.

– Recalculate the continuous phase flow by adding the interphase momentum exchange (equation (7)) determined during the previous particle calculation.

– Recalculate the discrete phase trajectories in the modified continuous phase flow field.

– Repeat the previous two steps until a converged solution is achieved.

When the discrete and continuous phase are being coupled, it is better to apply an under-relaxation scheme to the momentum exchange terms for improving the numerical stability of the coupled calculation procedure:

$$\boldsymbol{F}_{new} = \boldsymbol{F}_{old} + \alpha(\boldsymbol{F}_{calculated} - \boldsymbol{F}_{old}), \tag{8}$$

where the $\boldsymbol{F}_{new}$ is the momentum exchange term, $\mathbf{F}_{old}$ is the previous value, $\boldsymbol{F}_{calculated}$ is the newly computed value, and α is under-relaxation factor. Here $\alpha = 0.35$ is adopted in this study. Note that the value of α does not influence the predictions obtained in the final converged solution.

Numerical results and discussion

The extraction column is cylindrical. Due to the periodic property of the flow field, only the flow field shown in Figure 1, which is the extraction column with the circumference angle 120°, is calculated here. The geometric parameters of one extraction compartment are listed in Table 1. The cylindrical coordinates shown in Figure 2a are used everywhere in this paper.

Figure 1 shows two compartments of the extraction column with a cutting off at 3 mm distance in the compartment below. The intercepted part is combined with the above compartment to assure the periodic boundary at the inlet and outlet boundaries. The commercial CFD software FLUENT 5.5 is adopted in this study. A 52 × 38 × 128 ($r \times \theta \times z$)

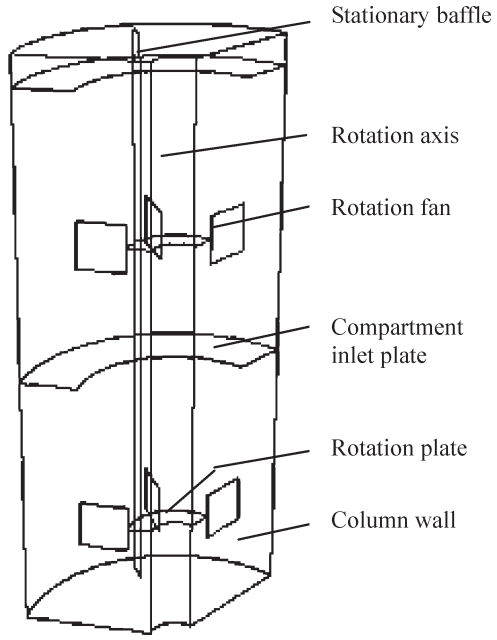

Fig. 1 – *The flow domain of an agitated extraction column*

Table 1 – *Geometric quantities of one extraction compartment (unit: mm)*

Diameter	Height	Inlet diameter of compartment	Diameter of inner rotation axis
32	28	20	4
Height of rotation fan	**Width of rotation fan**	**Width of baffle plate**	**Outer diameter of rotation plate**
4.5	5	2	10

grid arrangement is adopted here because of giving grid-independent results. At circumference direction, a circumference periodic boundary condition is used on the two cross-sections with a 120° circumference angle apart.

The flow field of the agitated extraction column is calculated by the multiple reference frame model (MRF), which is required to separate flow filed into the stationary and moving zones. This model is the simplest and has some advantages over the other models that can be used to simulate flows with rotators and baffles. Because of current limited computer resource and very long computer CPU time, required for simulating a two-phase extraction process, we take MRF in our computation to reduce greatly the computing time of each case. The results of MRF model may be in some kinds of approximation because a steady-state approximation is assumed in this model. But actually, the individual cell zones may be rotating at different rotational speeds. Of course, this approximation may cause a certain difference between the numerical results and the real flow field. And we believe that this difference will be small because the stationary baffle is not too close to the rotators such as the case in present study. Figure 3b shows the relative position of the rotator and baffle.

The continuous phase (water) is put at top boundary and the dispersed phase (toluene) is injected from the surface which is 21 mm above the below boundary. For all calculations presented here, the feed speed of continuous phase is 8 l h^{-1} downwards and the diameter and the injection speeds of dispersed phase (drops) are 1.2 mm and 4 cm s^{-1} if not specially mentioned.

Figure 2 shows the contours of continuous phase velocity magnitude at different cross-sections. It can be found out that the flow field of continuous phase is very complex and there are many vortexes with complex shapes. For simplification, only the vortexes, which are important to the flow property of extraction column, are mentioned here.

Figures 2a-2d show the structures of the six major vortexes in flow direction. The effects of stationary baffle may cause these vortexes. With increasing coordinate z, it can be found out that the vortexes are moving to the inner rotation axis. In Figure 2b, the vortexes attach to the rear of the rotators. After that, the vortexes move out to the outer column boundary and attach to the boundary as shown in Figure 2d.

Figures 2a-2d also indicate that a small circulation appears at the rear of the baffle.

Figures 2e-2h show the vortexes on four circumference direction cross-sections. The two strong vortexes around the rotators are due to the rotation of rotators. These two vortexes are moving periodically towards outer column boundary as they are far from the baffle and moving towards the inner rotation axis as they are closed to the baffle.

To view the flow velocity field of continuous phase more clearly, the data of Figure 2 is reproduced in another way. Figure 3 shows the low and high velocity areas in the extraction column more clearly compared with Figure 2. On z = 33 mm (see Figure 3a) and z = 45 mm (see Figure 3c) cross-sections, which are below and above the rotating fan, respectively, the velocity decreases at first, then increases and finally decreases to zero in order to satisfy the wall boundary condition with the increase of radial coordinate. The minimum velocity is corresponding to the center of vortex. On h = 38 mm (see Figure 3b) cross-section, which is just at the middle of rotator, the velocity increases to maximum value and then decreases to zero on the wall. The velocity on the rotating fan is linearly dependent on the radial coordinate. On h = 50 mm (see Figure 3d) cross-section, the velocity near the center is high because all liquid is attracted to the cen-

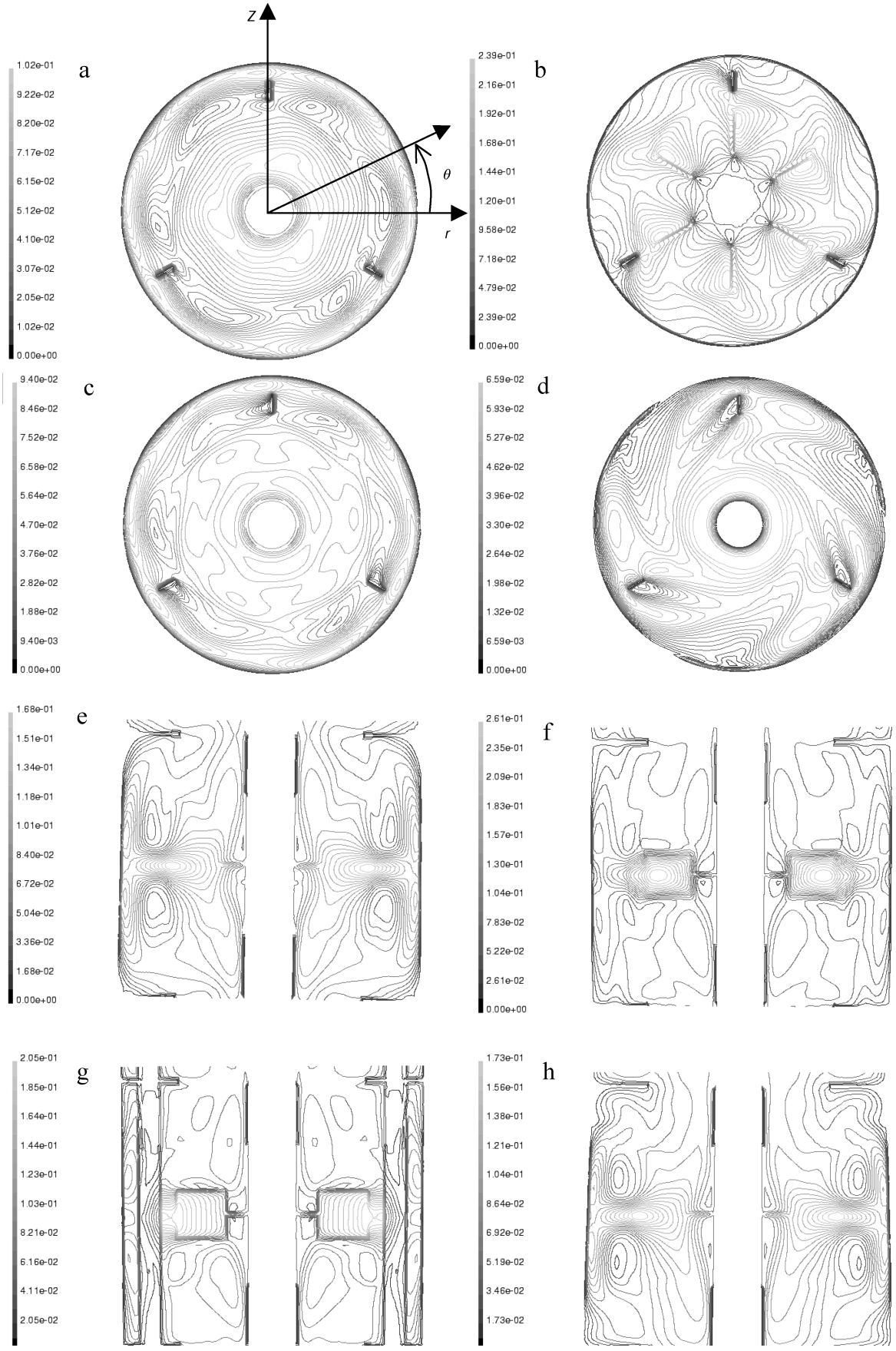

F i g . 2 – *Contours of velocity magnitude of continuous phase (m s^{-1}) for rotation speed 200 rpm on different cross-sections. Cases a, b, c, d are for z = 33, 38, 45, 50 mm cross-sections. Cases e, f, g, h are for circumference angle θ at 60, 85, 91, 120 cross-sections.*

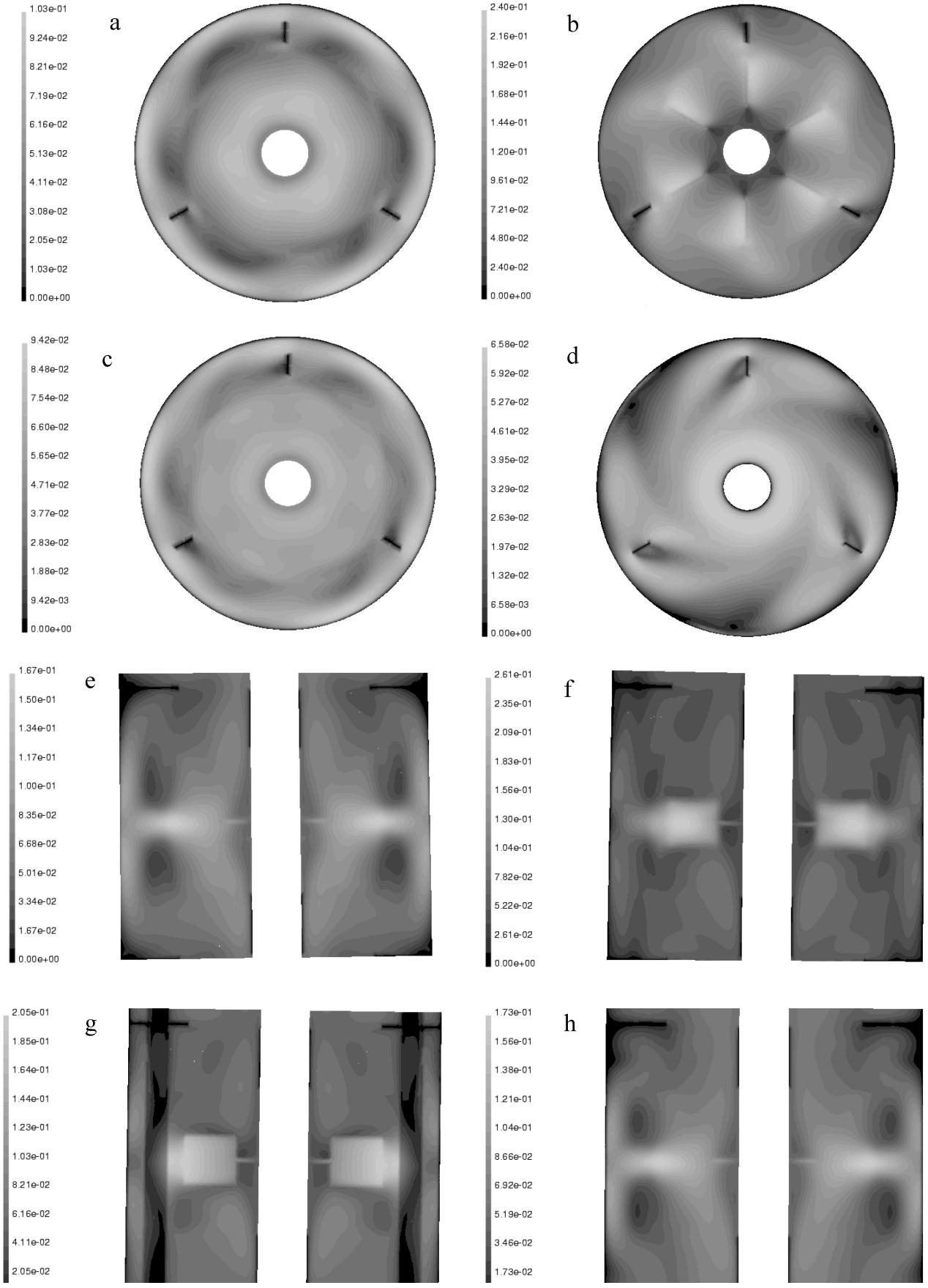

F i g . 3 – *Contours of velocity magnitude of continuous phase (m s^{-1}) for rotation speed 200 rpm on different cross-sections. Cases a, b, c, d are for z = 33, 38, 45, 50 mm cross-sections. Cases e, f, g, h are for circumference angle θ at 60, 85, 91, 120 cross-sections.*

ter and then flow downwards along the rotating inner cylinder. Figures 3e–3h show that the two counter-rotating vortexes around the rotator are strong when they are far from the baffle and are weak when they are near the baffle. On the side of baffle facing flow, the velocity of continuous phase is high and the flow (vortex) structure around baffle is very complex.

The contours of density concentration of dispersed phase on different cross-sections are shown in Figure 4 for rotating speed 200 rpm. The white areas in Figure 4 correspond to the high concentration areas of dispersed phase (toluene). Generally, the drops are moving under the combined effects of buoyancy and the flow of continuous phase. After the dispersed drops enter the extraction compartment (see Figures 4a and 4e–4h), the high concentration of dispersed drops below the fan are uprising to follow the inner rotating cylinder due to the vortex shown in Figure 3e. As the drops reach the fan, most of them are moving towards the outer column wall and uprising due to the combined effects from buoyancy and the stream of the vortex above the rotating fan. Only a few drops continue following the vortex stream below the rotating fan and they are finally stopped by the buoyancy effect as shown in Figures 4a and 4e. In the rotation speed 200 rpm case, the average holdup of dispersed phase in an extraction compartment is about 2.4 %.

The contours of density concentration of dispersed phase on different cross-sections are shown in Figure 5 for rotating speed 250 rpm. In Figure 5a, there is a high concentration of dispersed phase near the inner rotating cylinder. With the increase of radial coordinate, the concentration of dispersed phase reduces at first and then increases. The lower concentration area is corresponding to the center of vortex bellow the rotator. In Figure 5b, the distribution of dispersed phase is nearly uniform. Figure 5c shows the uprising drops are moving to the outer column wall. Figure 5d shows the distribution of dispersed phase is becoming uniform again and they are going towards the inner rotating axis with the vortex stream as moving upwards. And most of the dispersed phase is uprising and finally leaving the extraction compartment. Figures 5e–5h show the dispersed phase above the rotator can follow the vortex stream and complete a circle. This only happens when the rotating speed increases to 250 rpm. In this case, the average holdup of dispersed phase in an extraction compartment is about 2.7 %.

Figure 6 shows the density concentration contours of the dispersed phase on different cross-sections for rotating speed 150 rpm. The behavior of dispersed phase is similar to that shown in Figure 4. In this case, the average holdup of dispersed phase in an extraction compartment is about 1.9 %.

The effect of different particle drag law on the flow field is also discussed in this study. If a solid particle drag law ($C_D = \frac{24}{Re_p}(1 + 0.15\, Re_p^{0.687})$ see *Clift* et al.[10]) is used instead of the liquid drop drag law (see equation (5)), similar results to Figures 2–6 can be obtained under the same condition. The major difference between the results of these two drag laws is the average holdup of dispersed phase in an extraction compartment. For example, in the case of the rotating speed 250 rpm, the average holdup of dispersed phase in an extraction compartment for the solid particle drag law is about 3.8 %, and that is about 2.7 % for the liquid drop drag law. The reason for this difference is that the drag force acting on a liquid drop is smaller than that on a solid particle in the same condition. Then, the liquid drops will face little resistance and can move upwards faster to leave the extraction compartment in a shorter resident time. This causes the reduction of the average holdup of dispersed phase in an extraction compartment. The result also indicates that the average holdup of dispersed phase in an extraction compartment is very sensitive to the drag law adopted and a careful choice of suitable drag law is strongly required.

How do the injecting parameters of dispersed phase affect the concentration distribution of dispersed phase in an extraction compartment? The effects of the diameter and injecting velocity of dispersed phase are discussed. At the rotation speed of 150 rpm, the drop diameter is increased to 2 mm and the injection velocity is reduced to 2 cm s^{-1}. Numerical results show that the drops suffer stronger resistance comparing to former cases and form a high concentration area of dispersed phase under the compartment inlet plate. The average holdup of dispersed phase in an extraction compartment is increased to about 6.1 %. This phenomenon refers to flooding in a real operation. By this time, most of dispersed drops cannot get enough contact with the continuous phase and it results in very low mass transfer efficiency between two phases. Flooding should be avoided in extraction columns design.

Conclusions

The liquid-drop (water and toluene drops as an example here) two-phase flow is simulated by the Lagrangian-Eulerian method presented here. Numerical results show that Lagrangian-Eulerian method can be applied to study the flow field of liquid-liquid extraction column and furthermore this method has a high potential to include mass transfer between two phases. It can be further developed to

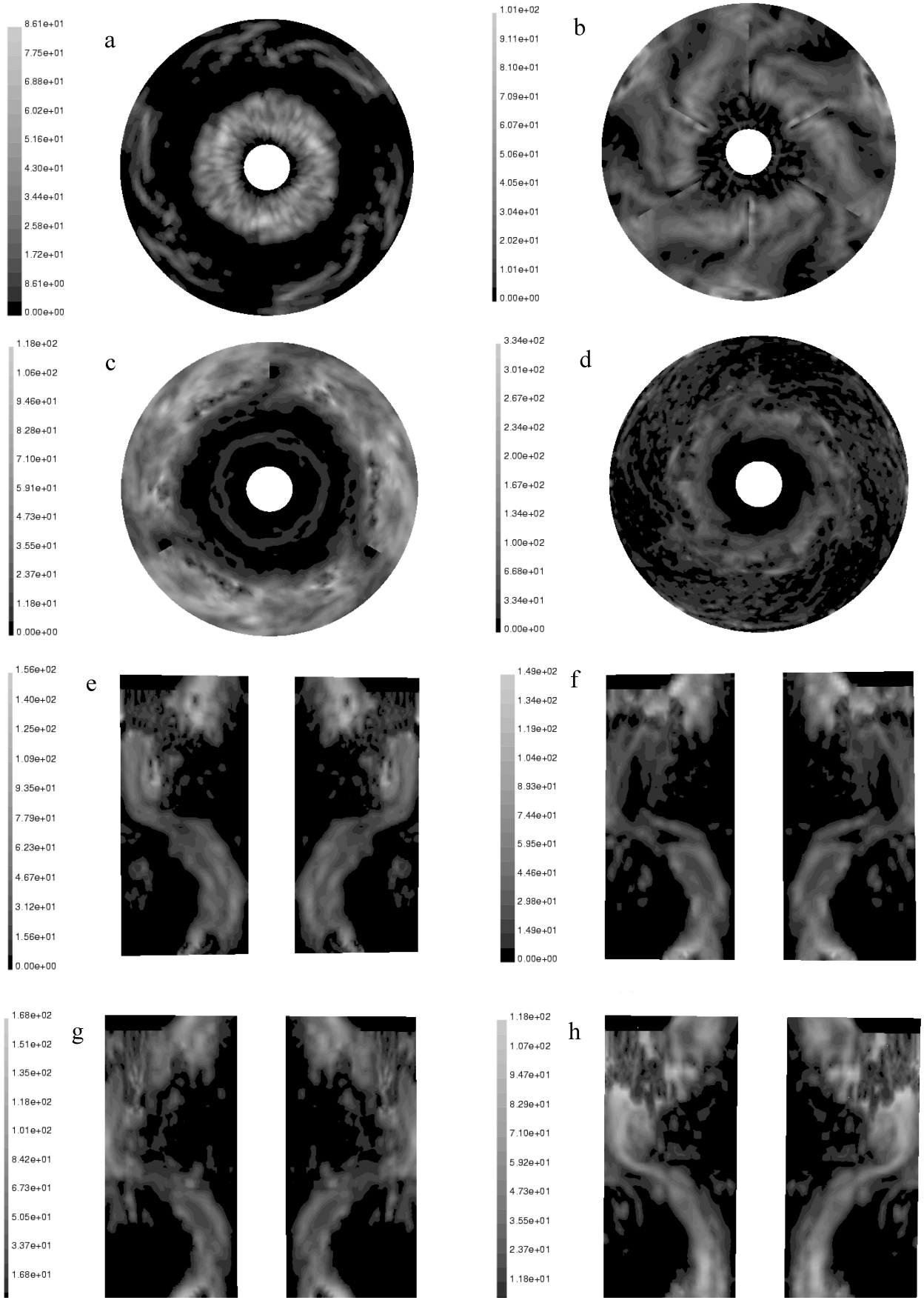

F i g . 4 – *Contours of density concentration of dispersed phase (kg m⁻3) for rotation speed 200 rpm on different cross-sections. Cases a, b, c, d are for z = 33, 38, 45, 50 mm cross-sections. Cases e, f, g, h are for circumference angle θ at 60, 85, 91, 120 cross-sections.*

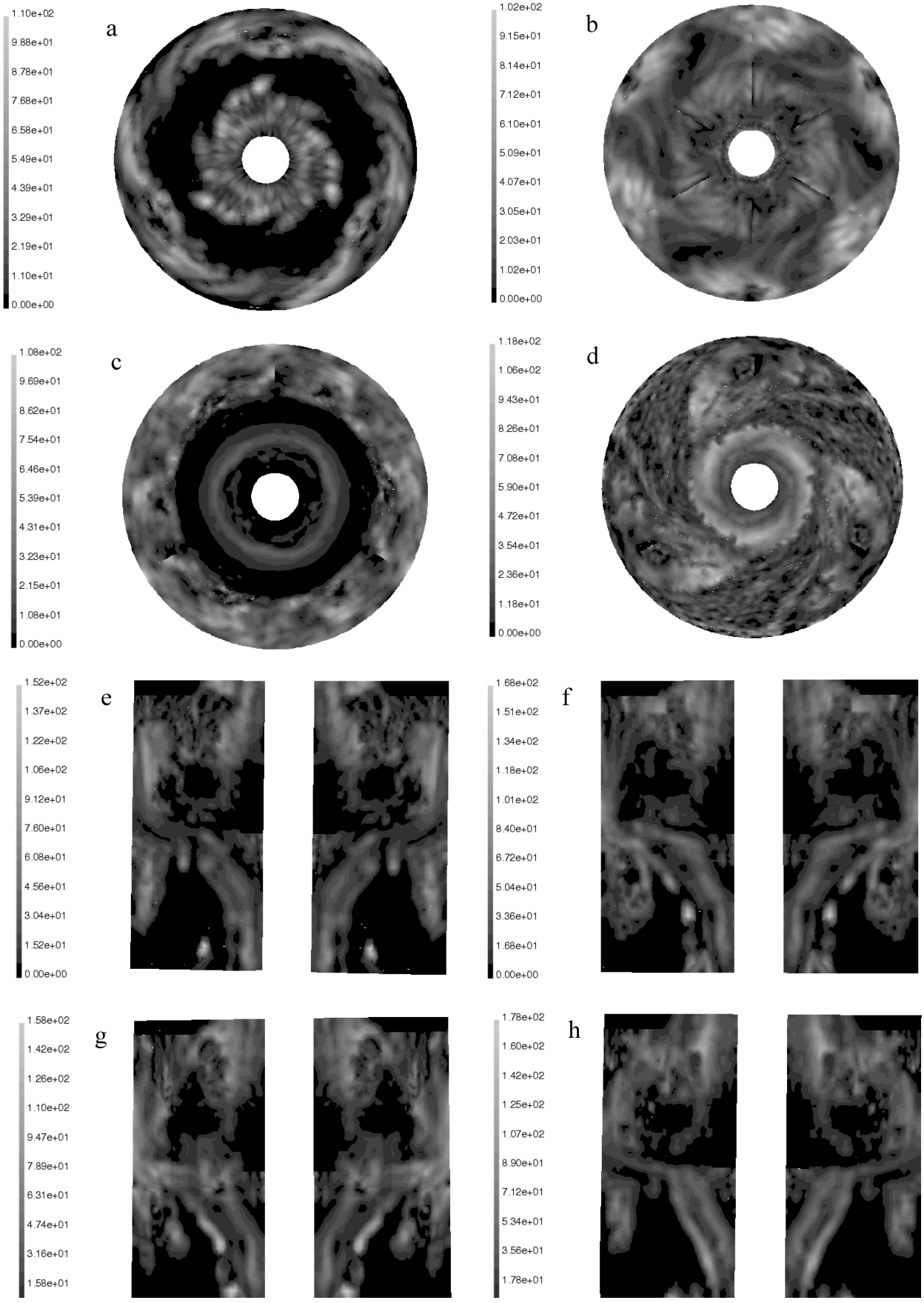

F i g . 5 – *Contours of density concentration of dispersed phase (kg m⁻3) for rotation speed 250 rpm on different cross-sections. Cases a, b, c, d are for z = 33, 38, 45, 50 mm cross-sections. Cases e, f, g, h are for circumference angle θ at 60, 85, 91, 120 cross-sections.*

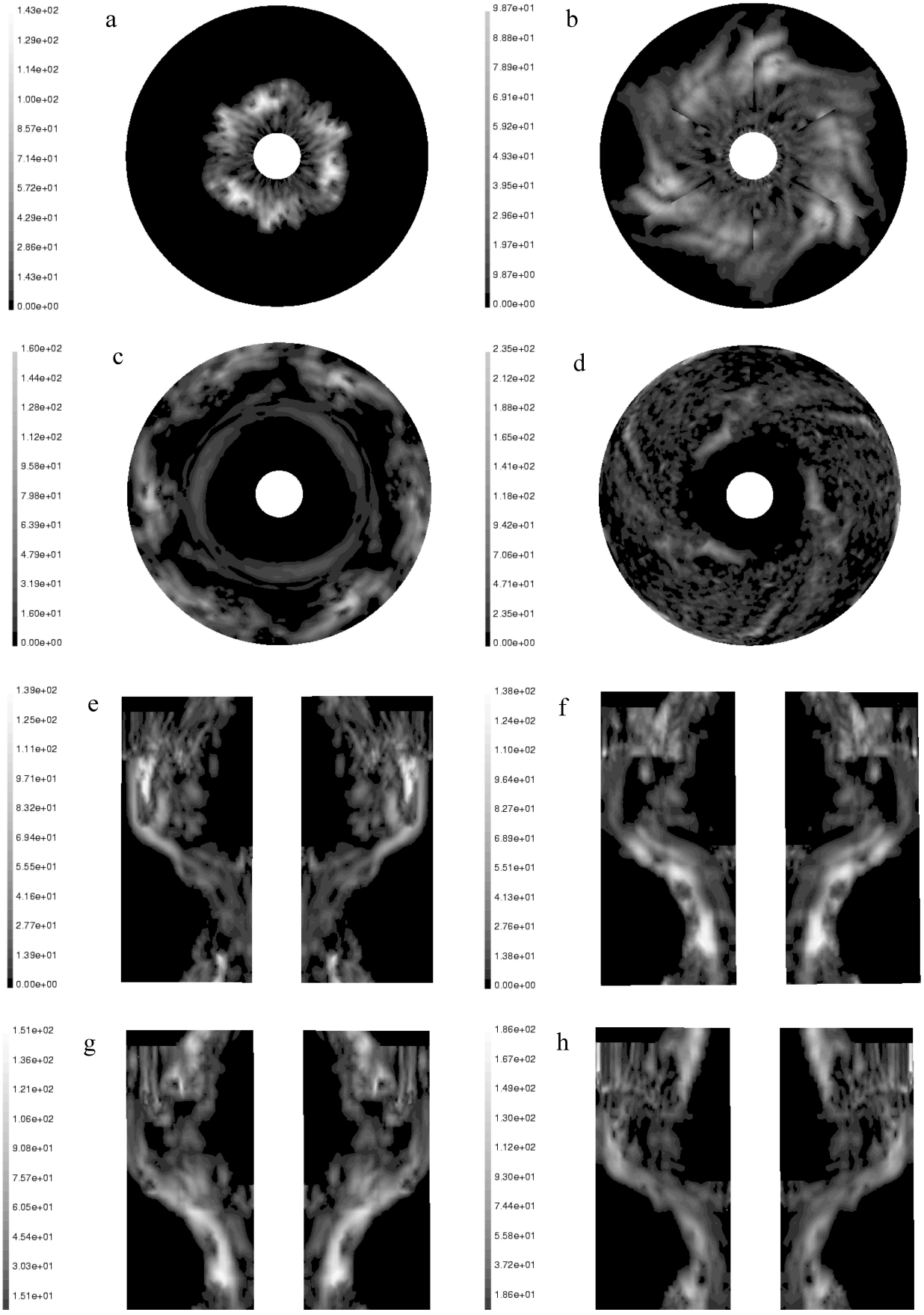

F i g . 6 – *Contours of density concentration of dispersed phase (kg m–3) for rotation speed 150 rpm on different cross-sections. Cases a, b, c, d are for z = 33, 38, 45, 50 mm cross-sections. Cases e, f, g, h are for circumference angle θ at 60, 85, 91, 120 cross-sections.*

study the efficiency and to optimize the performance of extraction column without any problems.

Numerical results suggest that adopting different drag laws of dispersed phase has very large influence on the distribution of dispersed phase and a careful choice of drag law is required. Numerical results also show that the rotation speed, the drop diameter, and injection velocity of dispersed phase can have strong influence on the distribution of dispersed phase. The above parameters should be optimized when designing high performance extraction columns. The geometry parameters of extraction column are not considered in this paper. Obviously, geometry parameters also have strong influence on the performance of extraction columns and these parameters can also be optimized by the Lagrangian-Eulerian method presented here.

Only a few cases studied here are not enough to get an optimized extraction column. More computing is still required. In order to reduce the cases of calculation, careful arrangements of operation and geometry parameters should be very much required. In the cases we studied, the case with the rotation speed of 250 rpm gives a better distribution of dispersed phase in the view of flow field. To search for an optimal extraction column, the mass transfer between two phases must be considered.

ACKNOWLEDGEMENTS

The authors would like to acknowledge Prof. H.–J. Bart from Universität Kaiserslautern (Germany) for many helpful discussions. The authors also thank for the support of the Scientific Research Foundation for the Returned Overseas Chinese Scholars, the State Education Ministry of China and 985 Research Fund of Tianjin University.

Nomenclature

C_D – drag coefficient
d_p – drop diameter
$\boldsymbol{F}$ – interaction force vector
$\boldsymbol{g}$ – gravity constant
Q_p – the mass flow rate of the particles
p – pressure
r, θ, z – cylindrical coordinates
Re – Reynolds number
t – time
$\boldsymbol{u}$ – velocity vector

Greek symbols

α – under-relaxation factor
ε – volume fraction
κ – viscosity ratio
ρ – density
μ – viscosity
Ω – rotation speed vector

Subscripts

p – dispersed phase
l – continuous phase
r, θ, z – coordinates component

References

1. *Krishna, R., Van Baten, J. M.,* Trans IchemE (Part A), **79** (2001) 283.
2. *Yu, K. T., Yuan, X. G., You, X. Y., Liu, C. J.,* Chem. Eng. Res. Des., **77** (1999) 554.
3. *You, X.Y.,* Chem. Biochem. Eng. Q. **18** (2004) 223.
4. *Fei, W. Y., Wang, Y. D., Wan, Y. K.,* Chem. Eng. J., **78** (2000) 131.
5. *Sun, H., Wang W., Mao, Z.,* Chinese J. Chem. Eng. **10** (2002) 15.
6. *Bartels, C., Breuer, M., Wechsler, F., Durst, F.,* Computers & Fluids **31** (2002) 69.
7. *You, X. Y., Bart, H.,* Chinese J. Chem. Eng. **11** (2003) 362.
8. *Wachem, B. G. M. van, Schaaf, J. van der, Schouten, J. C., Krishna, C. M., Bleek, C. M. van den,* Powder Tech., **116** (2001) 155.
9. *Li, Y., Zhang, J., Fan, Liang-Shih,* Chem. Eng. Sci. **54** (1999) 5101.
10. *Clift, R., Grace, J. R., Weber, M. E.,* Bubbles, Drops and Particles, Academic press, 1978.